Journal of Wind Engineering & Industrial Aerodynamics 252 (2024) 105814

Contents lists available at ScienceDirect

Journal of Wind Engineering & Industrial Aerodynamics

journal homepage: www.elsevier.com/locate/jweia

Influence of inflow acceleration on the aerodynamic characteristics of a square cylinder

G. Lunghi [a], S. Brusco [b,c], A. Mariotti [a,*], G. Piccardo [c], M.V. Salvetti [a]

[a] Dipartimento di Ingegneria Civile e Industriale, Università di Pisa, Largo Lucio Lazzarino 2, 56122 Pisa, Italy
[b] Boundary Layer Wind Tunnel Laboratory, Faculty of Engineering, University of Western Ontario, London, ON, Canada, N6A 5B9
[c] Dipartimento di Ingegneria Civile, Chimica e Ambientale, Scuola Politecnica, Università di Genova, Via Montallegro 1, 16145 Genova, Italy

ARTICLE INFO

Keywords:
Large-Eddy Simulations
Inflow acceleration
Square cylinder
Vortex-shedding frequency
Wavelet transform

ABSTRACT

Large-Eddy Simulations were conducted to investigate accelerated flows around a square cylinder. The study explores flow characteristics for Gaussian-type accelerations of the inflow within the range of Reynolds numbers $Re = 1.720 \times 10^4$ to $Re = 6.536 \times 10^4$. Three different inflow acceleration intensities within the same range of Re have been considered. For all analyzed acceleration values, time cells with a constant frequency in vortex shedding were identified in agreement with the experimental findings of Brusco et al. (2022a). The temporal behavior of the vorticity field indicates that vortex packets are shed at a constant frequency within these cells. Moving from one cell to another, there is a discontinuity in the vortex-shedding mechanism, leading to an unsteady but more symmetrical wake and a reduction in crossflow-force fluctuations. Subsequently, vortex shedding restarts at a higher frequency. As acceleration intensity increases, the time length of the constant-frequency time cells decreases. A similar behavior of the Strouhal number with the Reynolds number is obtained for all acceleration intensities.

1. Introduction

The analysis of wind effects on structures is typically associated with the Davenport Chain (Davenport, 1961). Within this framework, the transition from wind to a force field involves the application of strip theory and quasi-steady theory (e.g., Kawai, 1983). Strip theory is a simplification method that entails dividing a complex structure into small strips and analyzing the forces and moments acting on each strip individually. Quasi-steady theory, on the other hand, assumes that the aerodynamic forces acting on a structure respond almost instantaneously to changes in wind conditions. In other words, it considers the forces to be in quasi-equilibrium with the changing wind, simplifying the analysis. This assumption involves considering a memory-less system, implying the neglect of unsteady effects when defining the force field (Kareem and Wu, 2013). This well-established hypothesis is suitable for designing structures to withstand synoptic winds (e.g., Solari, 2019), whose steady characteristics can be replicated through static wind-tunnel tests and numerical simulations, both conducted under constant inflow conditions.

The characteristics of the flow and the aerodynamic loads acting on spanwise-elongated bluff bodies with simple geometry under steady inflow conditions have been extensively investigated in the literature. A classical example is the flow around a square cylinder of infinite spanwise length (Vickery, 1966; Bearman and Obasaju, 1982; Lyn et al., 1995; Rodi et al., 1997; Rodi, 1997; Sohankar et al., 1999; Saha et al., 2003; Minguez et al., 2011; Trias et al., 2015; Bruno and Oberto, 2022). Moreover, the dependence of the measured values of the pressure and force coefficients on the sharpness of the edges was investigated in Tamura and Miyagi (1999), on the free-stream turbulence in Roberson et al. (1972), Lee (1975), Tamura and Miyagi (1999), Petty (1979), Nakamura and Ohya (1984), Durão et al. (1988), Lyn and Rodi (1994) and on the Reynolds number in Norberg (1993), Chen and Liu (1999).

On the other hand, understanding the impact of non-synoptic winds, such as thunderstorm outflows or tornadoes, on the aerodynamics of bluff bodies remains a challenging task, even for the most classical configurations. This challenge arises from the historical lack of full-scale data, which is hindered by the limited time duration of these events and the confined size of the storm covering a much smaller area than a typical cyclonic one. Additionally, reproducing the dynamic features of non-synoptic winds in a laboratory or through numerical simulations is highly complex (refer, for instance, to the WindEEE Dome facility at the University of Western Ontario in Romanic et al.,

---

* Corresponding author.

E-mail addresses: gianmarco.lunghi@phd.unipi.it (G. Lunghi), sbrusco@uwo.ca (S. Brusco), alessandro.mariotti@unipi.it (A. Mariotti), giuseppe.piccardo@unige.it (G. Piccardo), maria.vittoria.salvetti@unipi.it (M.V. Salvetti).

https://doi.org/10.1016/j.jweia.2024.105814
Received 5 December 2023; Received in revised form 13 June 2024; Accepted 28 June 2024

2021; Kopp and Wu, 2020). As a result, most of the existing literature offers analyses of structural responses to non-stationary flows under the assumption of stationary inflow conditions, lacking a reference database for accelerating or decelerating flows. Nevertheless, in recent years there has been a notable increase in research activities aimed at exploring the distinctive features of flows associated with non-synoptic winds, specifically the flow acceleration, and comprehending its impact on structural performance. Notably, flow acceleration has the potential to challenge the applicability of strip and quasi-steady theories (e.g., Kwon and Kareem, 2019). On one hand, acceleration is linked to the generation of forces, such as Froude–Krylov force, which are absent in steady flows and thus are usually disregarded in a conventional quasi-steady approach (e.g., Brusco et al., 2022b). On the other hand, flow acceleration may directly influence the characteristics of separating boundary layers, as well as the geometry of potential separation bubbles and wake recirculation regions. These features may significantly differ from those defined under steady conditions.

With respect to the transient aerodynamics of slender bodies, Sarpkaya (1963, 1966) observed a 25% increase in the drag coefficient of a circular cylinder when the flow was impulsively started, compared to the value obtained under steady conditions. Sarpkaya and Kline (1982), Sarpkaya and Ihrig (1986) investigated different bodies and observed the overshooting of the drag coefficient for spanwise-elongated bodies at small incidences, while the square cylinder did not exhibit any overshooting for the same orientation. Studies by Takeuchi et al. (2008), Takeuchi and Maeda (2013) generated step-function-like flows to examine a railcar-like body, finding overshooting in both drag and lift directions when the initial flow state was non-quiescent. However, as noted by Yang and Mason (2019), the flow accelerations and, consequently, the model scale inertial forces reproduced in the former experiments are at least one order of magnitude higher than those representative of thunderstorm-induced conditions for typical geometries of civil structures. This is reflected in a mismatch of acceleration parameters, aD/u_∞^2, where a and u_∞ are the flow acceleration and velocity, respectively, and D is the dimension of the body in the along-wind direction. Yang and Mason (2019) reproduced more realistic values of the acceleration parameters for spanwise-extruded square and rectangular cylinders (aspect ratios equal to 1:3, 1:1, 3:1) at zero flow incidence. Based on their results, they considered an increase in the load beyond what was experienced at the same wind velocity in steady conditions as unlikely. Computational Fluid Dynamics (CFD), particularly Large-Eddy Simulations (LES), serves as a valuable tool for gaining insights into the dynamic evolution of the flow field under accelerating and decelerating conditions. A notable example of this application is evident in the work of Guo et al. (2021), who investigated the characteristics of the flow field and wind loads on a square cylinder. The study focused on a range of Reynolds numbers, denoted as $Re = u_\infty D/\nu$ with ν being the kinematic viscosity of air, spanning from 0 (representing a quiescent condition) to 5×10^4. The acceleration profile applied was a constant acceleration, expressed as $aD/u_\infty = 0.0048$. Moreover, numerical studies on accelerated flows have encompassed not only sectional geometries but also three-dimensional bodies relevant to civil engineering (Li et al., 2023) and the transportation sector (Zhou et al., 2023).

Within the ERC Project THUNDERR (Solari, 2020), Brusco et al. (2022a) conducted an experimental campaign to examine the impact of a Gaussian-type acceleration on a square cylinder at zero angle of attack, spanning Reynolds numbers (Re) from 1.720×10^4 to 6.536×10^4. Analysis of pressure and force signals revealed that the vortex shedding frequency under transient conditions does not consistently track the variation in wind speed. Instead, they are characterized by constant-frequency time cells with discontinuity in the transition from one to another. These discontinuities correspond to a sudden decrease in mean aerodynamic drag and fluctuating lift coefficient (Brusco et al., 2024). This current study aims to replicate, through LES, the same inflow acceleration conditions as the experimental campaign in Brusco et al. (2022a) for cross-comparison. Multiple numerical probes are strategically positioned on the body's surface, enabling a direct comparison of numerical pressure measurements with those obtained from experiments. Furthermore, taking advantage of the detailed information on the flow dynamics provided by LES, the study aims to enhance understanding of vortex-shedding features, in particular, when discontinuous frequency changes occur. Finally, the investigation seeks to broaden the analysis in Brusco et al. (2022a) by conducting a parametric study that reproduces higher acceleration intensities than those reproduced in the experimental campaign. All these cases are in-depth investigated through the application of time–frequency analysis. The results of the present study may be useful for predicting potential aeroelastic phenomena resulting from vortex shedding induced by flow conditions typical of thunderstorm outflows on civil structures or structural elements.

We have structured the paper as follows: Section 2 details the numerical methodology and simulation set-up, whereas Section 3 introduces the non-dimensional coefficients and the time–frequency analysis procedure. In Section 4 we compare numerical results with experimental data. Section 5 delves into a comprehensive analysis of the vortex-shedding phenomenology in the context of accelerating flow around a square cylinder. The influence of acceleration intensity is discussed in Section 6, whereas the comparison between constant acceleration and Gaussian-type acceleration is presented in Section 7. Lastly, Section 8 provides some conclusive remarks.

2. Numerical methodology and simulation set-up

We conduct LES to investigate the incompressible, high-Reynolds number flow around a square cylinder at zero angle of attack. LES simulations are performed utilizing the Nek5000 code, which is a massively-parallel open-source solver designed for solving the incompressible Navier–Stokes equations based on a high-order spectral element method (Fischer and Mullen, 2001). The spectral elements utilized are rectangular, with Nth order Legendre polynomials for velocity and $(N-2)$th order for pressure serving as the basis functions within each element. For our investigations, we have opted for $N = 6$, consistent with previous studies (Mariotti et al., 2017; Lunghi et al., 2022). The method demonstrates spectral convergence in N (p-refinement) and converges with the accuracy of a high-order finite-element method in the number of elements (h-refinement). Time discretization is accomplished using the high-order splitting method developed by Maday et al. (1990). In particular, time derivatives are computed using a 3rd-order backward differentiation scheme. The viscous terms are treated implicitly, while a 3rd-order forward extrapolation in time is employed for non-linear convective terms. The non-dimensional time step remains consistent at 0.003, following the approach in Mariotti et al. (2017).

The stability of the spectral-element method is enhanced by incorporating an explicit low-pass filter in the modal space at the conclusion of each Navier–Stokes time integration (Fischer and Mullen, 2001). The applied modal filter is a sharp cut-off for modes up to the unfiltered mode (k_c), dampening the highest resolved modes ($k_c \le k \le N$) with a quadratic transfer function. This damping serves as a form of SubGrid Scale (SGS) dissipation (Domarazdki, 2010). Moreover, the degree of introduced dissipation can be adjusted using a weighting parameter, w. The filter transfer function is summarized as follows:

$$\begin{cases} \sigma_k = 1 & k < k_c \\ \sigma_k = 1 - w\left(\frac{k-k_c}{N-k_c}\right)^2 & k_c \le k \le N \end{cases} \tag{1}$$

The cut-off mode k_c is set to $N-3$, following the approach in Lunghi et al. (2022). The choice of the weighting parameter is informed by the sensitivity analysis results in Mariotti et al. (2017), with a selected value of $w = 0.05$, consistently with Rocchio et al. (2020).

The computational domain is illustrated in Fig. 1, with dimensions spanning $-75 \le x/D \le 125$, $-75 \le y/D \le 75$, and $-2.5 \le z/D \le 2.5$,

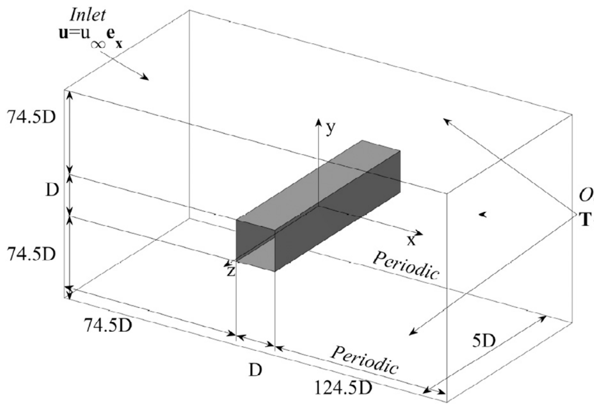

Fig. 1. Computational domain and reference system.

Table 1
Summary of the cases having Gaussian-type accelerations with different intensities.

Case	Acceleration		Non-dimensional time length
	$\max(aD/u^2_{\infty,0})$	$\max(aD/u^2_{\infty})$	
A	2.23×10^{-2}	7.6×10^{-3}	600
B	2.97×10^{-2}	1.01×10^{-2}	450
C	4.46×10^{-2}	1.51×10^{-2}	300

where x, y, and z represent the streamwise, crossflow, and spanwise directions, respectively. The side length of the square cylinder, denoted as D, serves as the reference length, and the reference system's center aligns with the cylinder's center at $x = y = 0$. The distribution and size of computational elements follow the typical structure for flows around similar geometries (Mariotti et al., 2017; Rocchio et al., 2020; Lunghi et al., 2022). Specifically, the element size is uniform at $\Delta z/D = 0.558$ in the spanwise direction. The element size in the streamwise direction is initially $\Delta x/D = 0.125$ near the cylinder ($-1 \leq x/D \leq 1$). Subsequently, a growth rate of 1.05 is applied in the range $-3 \leq x/D < -1$ and $1 < x/D \leq 10$. Finally, a growth rate of 1.1 is implemented for $x/D < -3$ and $x/D > 10$. Concerning the crossflow direction, the spacing $\Delta y/D = 0.125$ is maintained in the range $-1 \leq y/D \leq 1$. A growth rate of 1.05 is applied for $-2.5 \leq y/D < -1$ and $1 < y/D \leq 2.5$, while a growth rate of 1.5 is employed for $y/D < -2.5$ and $y/D > 2.5$.

Regarding boundary conditions, no-slip is enforced on the solid walls, and traction-free conditions are applied at the outflow. Periodicity is implemented in the spanwise directions. At the inlet, a uniform unsteady smooth-flow velocity (without turbulence) is imposed.

The inflow Reynolds number varies within the range of $Re = 1.720 \times 10^4$ to $Re = 6.536 \times 10^4$. Three different acceleration intensities are considered in the present study, as summarized in Table 1. The reference case that numerically reproduces the experiment in Brusco et al. (2022a) is here denoted as case A. The time histories of the inflow Re are reported in Fig. 2a. The behavior of the acceleration in time, $aD/u^2_{\infty,0}$, made non-dimensional by the inlet velocity at time $t = 0$, is reported in Fig. 2b; on the other hand, Fig. 2c shows the acceleration made non-dimensional by the instantaneous inlet velocity, aD/u^2_{∞}. The three cases analyzed all cover the same Reynolds-number range, but in different time lengths. Case B is obtained by reducing the non-dimensional time length of case A by a factor 3/4, and the case C by a factor 1/2. Consequently, case B has a maximum acceleration increased by 1.33 compared to case A, while case C is characterized by a double acceleration. All the accelerations start at $tu_\infty/D = 200$ with a flow that has reached developed-flow conditions at $Re = 1.720 \times 10^4$.

Finally, we investigate the effect of a constant acceleration by carrying out an additional simulation in which the velocity increases linearly between $Re = 1.720 \times 10^4$ and $Re = 6.536 \times 10^4$ over the same time range as in Case A. The time histories of the inflow Reynolds number and acceleration normalized by the inflow velocity at $t = 0$ are reported in Figs. 3a and 3b, respectively.

3. Definition of the quantities of interest and of the time-frequency analysis procedure

With respect to the quantities of interest, the coefficients for streamwise force and crosswind force (also referred to as the drag and lift coefficients hereafter) are defined as:

$$C_D = \frac{F_x}{\frac{1}{2}\rho u^2_\infty S} \tag{2}$$

$$C_L = \frac{F_y}{\frac{1}{2}\rho u^2_\infty S} \tag{3}$$

where F_x represents the streamwise force, F_y is the crosswind force, u_∞ denotes the free-stream velocity, ρ is the fluid density, and S represents the reference area.

The spanwise midsection of the cylinder is equipped with numerical probes to examine the time histories of pressure signals. The pressure coefficient, denoted as C_p, is defined by the equation:

$$C_p = \frac{p - p_\infty}{\frac{1}{2}\rho u^2_\infty} \tag{4}$$

where p represents the local pressure and p_∞ denotes the free-stream pressure.

Additionally, we introduce the streamwise differential-pressure coefficient, $C_{\Delta P_D}$, and the crossflow differential-pressure coefficient, $C_{\Delta P_L}$, following the notation in Brusco et al. (2022a, 2024). Referring to Fig. 4:

$$C_{\Delta P_D} = C_p^{\mathrm{fp}} - C_p^{\mathrm{rp}} \tag{5}$$

$$C_{\Delta P_L} = C_p^{\mathrm{tp}} - C_p^{\mathrm{bp}} \tag{6}$$

where C_p^{fp} and C_p^{rp} represent the pressure coefficients evaluated at the front and rear stagnation points, while C_p^{tp} and C_p^{bp} represent the pressure coefficients at the central points of the top and bottom sides of the square cylinder. These coefficients are associated with streamwise and crosswind loads. However, unlike the latter, they are assessed on a single streamwise section rather than on the entire body.

Time–frequency analysis of the pressure and force signals is conducted using wavelet maps with the complex Morlet wavelet, $\Psi(t) = e^{i\omega_0 t}e^{-t^2/2}$. The wavelet energy map is utilized to extract the main components modulated in frequency and amplitude for each signal through wavelet ridges, as detailed in Carmona et al. (1998), Buresti et al. (2004), Mariotti (2018). To derive the dominant frequencies, the signal undergoes transformation using a Morlet wavelet. Energy maps associated with each frequency over time are obtained, and the ridges are extracted by taking the maxima for each time. In this process, a high value of the central frequency of the wavelet, i.e., $\omega_0 = 6\pi$, is employed, to ensure high frequency resolution and minimize interference effects between adjacent components. For additional details, please refer to the procedure described in Brusco et al. (2022a).

4. Analysis of the results for the case A and comparison with the experiments

We compare the numerical results for Case A with the experiments conducted by Brusco et al. (2022a). Firstly, the time histories of the crossflow differential-pressure coefficient, $C_{\Delta P_L}$, and the crossflow force coefficient, C_L, are presented in Figs. 5a and 5c, along with the associated probability density functions (pdf) in Figs. 5b and 5d. Excellent agreement is observed between the numerical results and the experimental findings. The results for the crossflow differential-pressure coefficient and for the crossflow force coefficient well agree

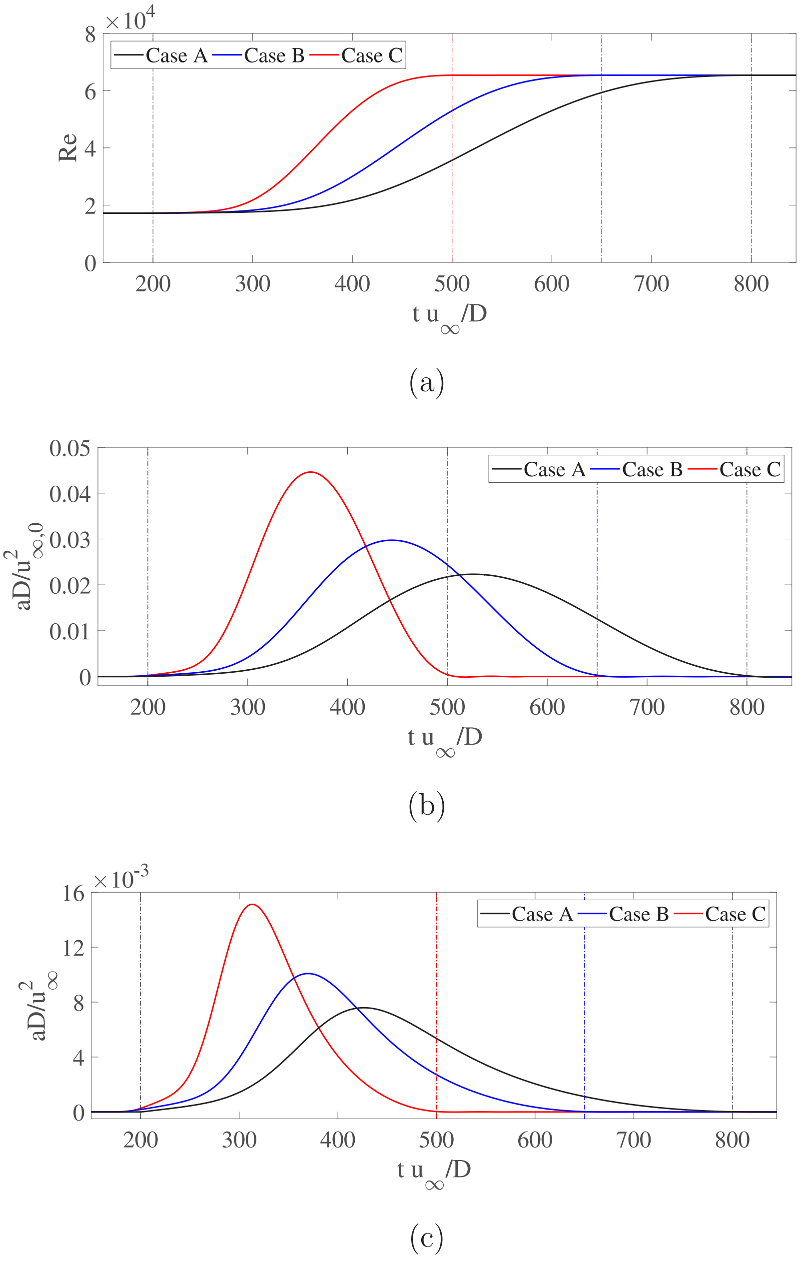

(a)

(b)

(c)

Fig. 2. Time histories of (a) inflow Reynolds number, (b) non-dimensional inflow acceleration normalized by the inflow velocity at $t = 0$, and (c) non-dimensional inflow acceleration normalized by the instantaneous inflow velocity. In all cases, the acceleration region is bounded by two vertical dash-dotted lines.

also in terms of pdfs. The periods of oscillations in $C_{\Delta P_L}$ and C_L decrease with increasing inflow velocity, indicating an increase in the vortex-shedding frequency. As the inflow velocity increases, multiple amplitude drops in the crossflow differential-pressure and force coefficients occur. Each drop is succeeded by the restarting of the oscillatory conditions with a higher frequency.

The time histories of the streamwise differential-pressure coefficients, $C_{\Delta P_D}$, and the streamwise-force coefficient, C_D, are presented in Figs. 6a and 6c, respectively. LES results show a global good agreement with the experiment. However, the streamwise differential-pressure coefficient, $C_{\Delta P_D}$, exhibits a higher time-average value in the simulation than in the experiment, and its standard deviation significantly widens. The maximum of the probability density function of the streamwise differential-pressure coefficient is obtained for higher values of $C_{\Delta P_D}$ in the simulations compared to the experiments, and the pdf is wider. Similarly, for the streamwise-force coefficient, higher resistance values are observed in the simulations than in the experiments, while the width of the distribution remains approximately the same. Indeed, the time-averaged value for C_D in simulations is equal to $\overline{C_{D,\mathrm{sim}}} = 2.19$, whereas in experiments, it is $\overline{C_{D,\mathrm{exp}}} = 2.06$. This difference could be attributed to the turbulence level in the wind tunnel (approximately 2%), while simulations are carried out for smooth flow. Similar values for the mean streamwise-force coefficient of the square cylinder for smooth inflow conditions are also reported in Bearman and Trueman (1972) and Sohankar (2006). As for the amplitude of fluctuations, the values found are similar to the ones in Sohankar (2006) and, it should be noted that the higher turbulence intensities in experiments may reduce the fluctuation amplitudes (Tamura and Miyagi, 1999). Moreover, to assess whether the differences between the simulations and the experimental findings in Brusco et al. (2022a) could arise from the spatial averaging over the taps of experimental pressure signals compared with numerical data from a single-point probe, we also computed numerical pressure signals by spatially averaging the pressure over a circle with a diameter equal to that of the pressure

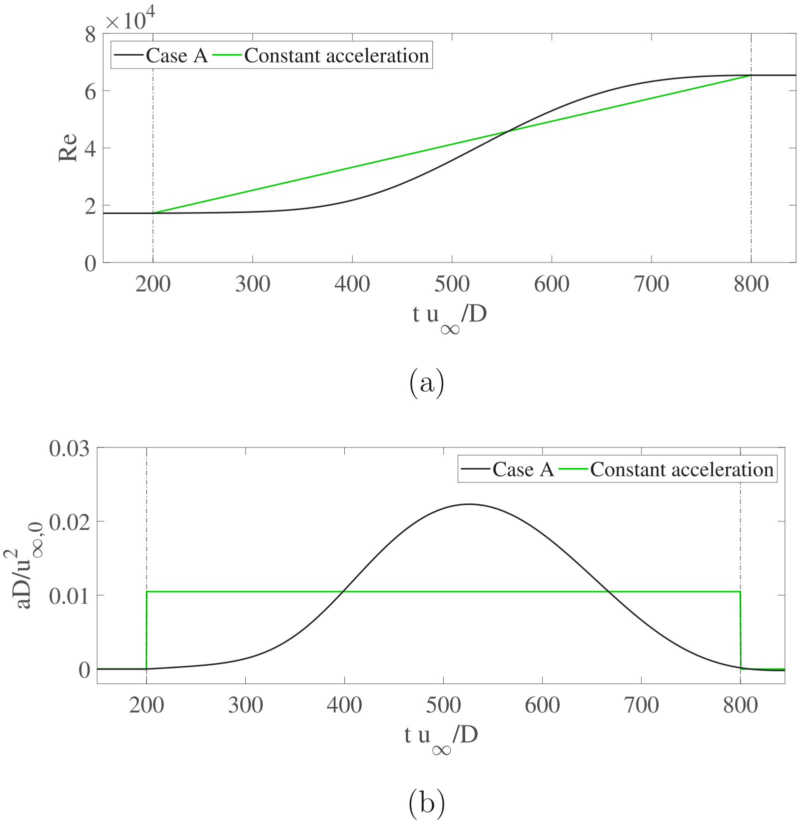

Fig. 3. Time histories of (a) inflow Reynolds number, and (b) non-dimensional inflow acceleration normalized by the inflow velocity at $t = 0$: comparison between reference Gaussian-type acceleration (Case A) and the constant acceleration.

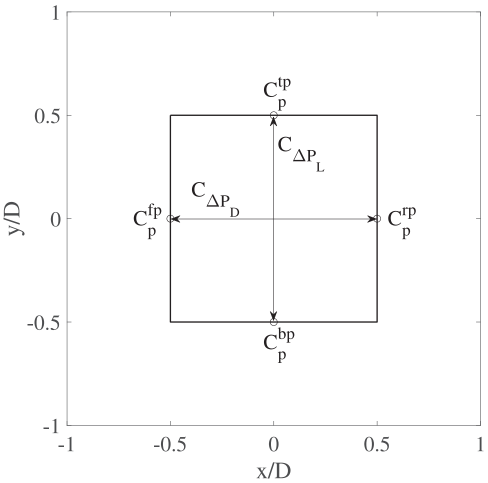

Fig. 4. Location of pressure probes at section $z/D = 0$ utilized for computing streamwise and crossflow differential-pressure coefficients.

taps used in the experimental tests, i.e., a circle with a diameter of 0.025D. Utilizing the spatially-averaged pressure value results in a slight reduction of signal oscillations in simulations, and, consequently, the pdf width slightly decreases. However, this alone is not sufficient to account for the discrepancy between the numerical and experimental outcomes.

The behavior of the vortex shedding frequency is now characterized through the time–frequency wavelet analysis. In Fig. 7a, the energy map of the wavelet transform of the $C_{\Delta P_L}$ signal is illustrated. From this map, we extract the vortex-shedding frequency n^* through the ridge analysis. We compare the ridges of the wavelet energy maps for the $C_{\Delta P_L}$ and C_L signals in Fig. 7b, and the same results in terms of dominant frequencies over time are found. Excellent agreement is also present between numerical and experimental results (Fig. 8a) for $C_{\Delta P_L}$ signals. Time cells with a consistent frequency in vortex shedding can be clearly identified. The vortex-shedding frequency increases stepwise during inflow accelerations. Indeed, sudden and incremental frequency variations are evident in the ridges of the $C_{\Delta P_L}$ and C_L signal. These discontinuities appear several times in the $C_{\Delta P_L}$ and C_L signals, and they are more pronounced closer to the maximum acceleration. Moreover, the time length of constant-frequency cells varies: it shortens when the velocity variation is greater. Consequently, having time cells with a constant frequency of vortex shedding leads to a non-constant Strouhal number, $St = n^* D/u_\infty$, since the instantaneous inflow velocity continuously increases. As can be seen in Fig. 8b, the St number decreases within the time cells in the range $0.10 \leq St \leq 0.14$, whereas the expected Strouhal number for constant inflow conditions and this Reynolds number range is $St \simeq 0.12$ (e.g., Bruno and Oberto, 2022).

5. Insight on the physical phenomenology of the accelerating flow

We analyze the temporal evolution of the spanwise vorticity ω_z on the plane $z/D = 0$ (Fig. 9 and the supplementary video) and the isocontours of the instantaneous vortex indicator λ_2 (Jeong and Hussain, 1995) (Figs. 10 and 11) during inflow accelerations to describe the changes in flow topology associated with the abrupt variations in vortex-shedding frequency discussed in Section 4. Figs. 9, 10, and 11 illustrate six specific time instants: (i) $tu_\infty/D = 250.5$, (ii) $tu_\infty/D = 403.5$, (iii) $tu_\infty/D = 486.0$, (iv) $tu_\infty/D = 559.2$, (v) $tu_\infty/D = 618.1$, and (vi) $tu_\infty/D = 692.9$. With reference to Fig. 9a, we selected three instants when the oscillations of C_L are clearly visible (i, iii, and (v), and three instants when the fluctuations of C_L significantly decrease (ii, iv, and (vi). The spanwise component of the vorticity field (Fig. 9b) clearly highlights an interruption in the alternate vortex shedding for

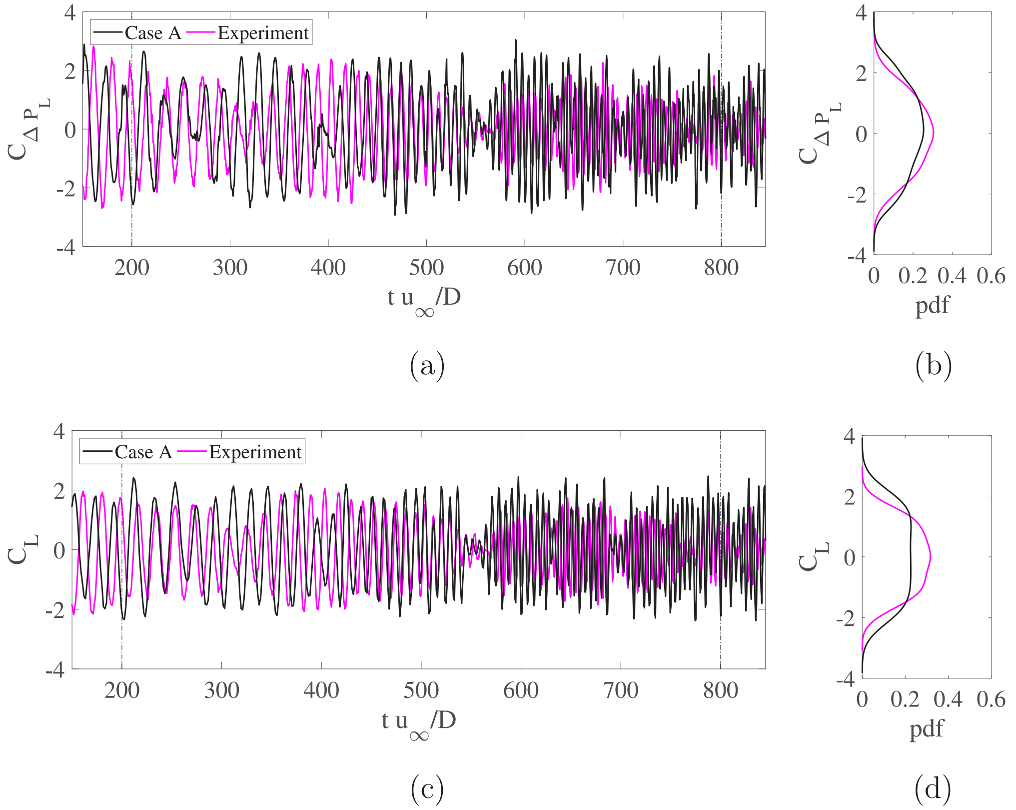

(a) (b)

(c) (d)

Fig. 5. Time histories of (a) crossflow differential-pressure coefficient, (b) along with the corresponding probability density function, and (c) crossflow force coefficient, (d) along with the associated probability density function during accelerating flow in Case A. The experimental data is sourced from Brusco et al. (2022a).

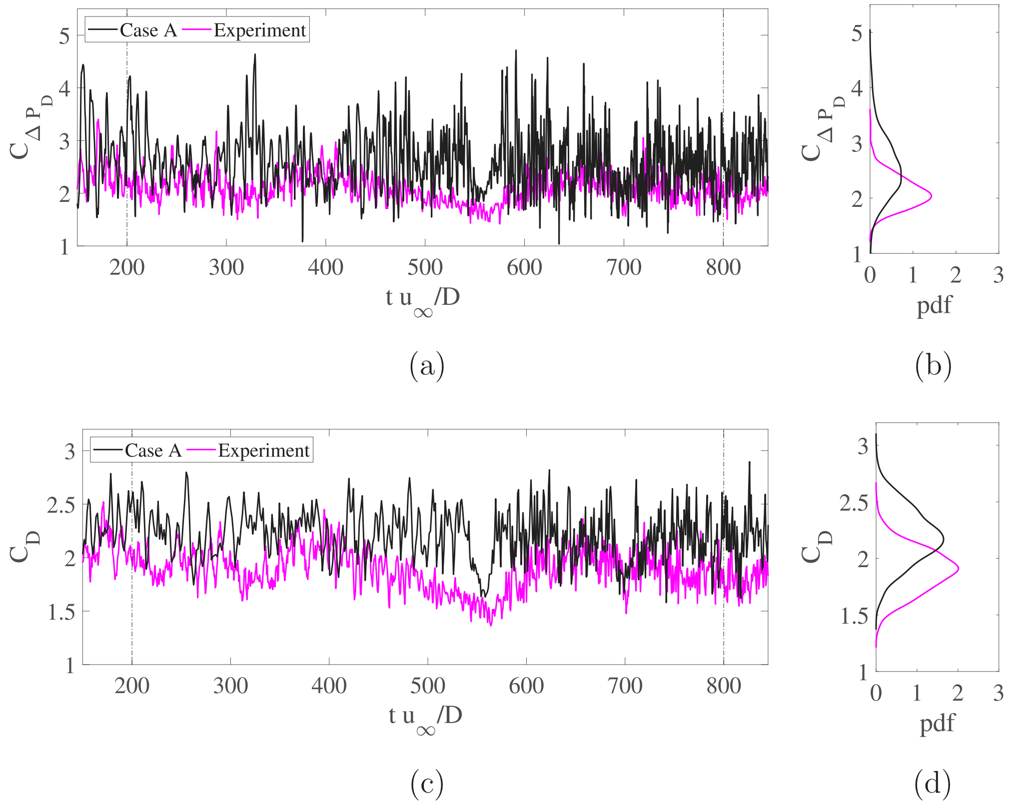

(a) (b)

(c) (d)

Fig. 6. Time histories of (a) streamwise differential-pressure coefficient, (b) along with the corresponding probability density function, and (c) streamwise force coefficient, (d) along with the associated probability density function during accelerating flow in Case A. The experimental data is sourced from Brusco et al. (2022a).

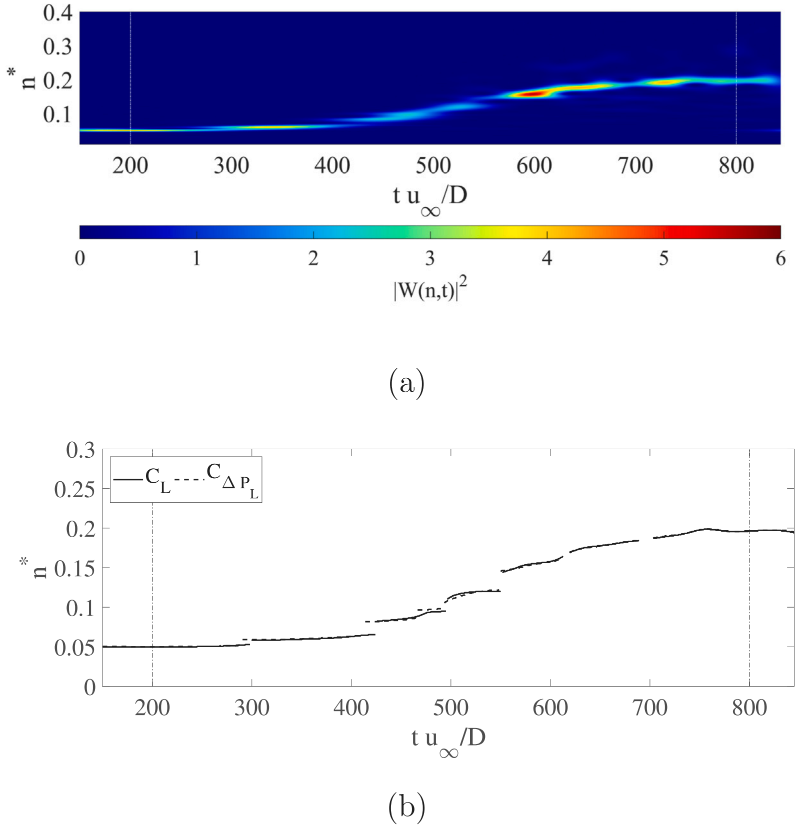

Fig. 7. (a) Wavelet energy map of $C_{\Delta P_L}$ signal during the accelerating flow in Case A. (b) Comparison of the ridges of the wavelet energy maps of $C_{\Delta P_L}$ and C_L signals for Case A.

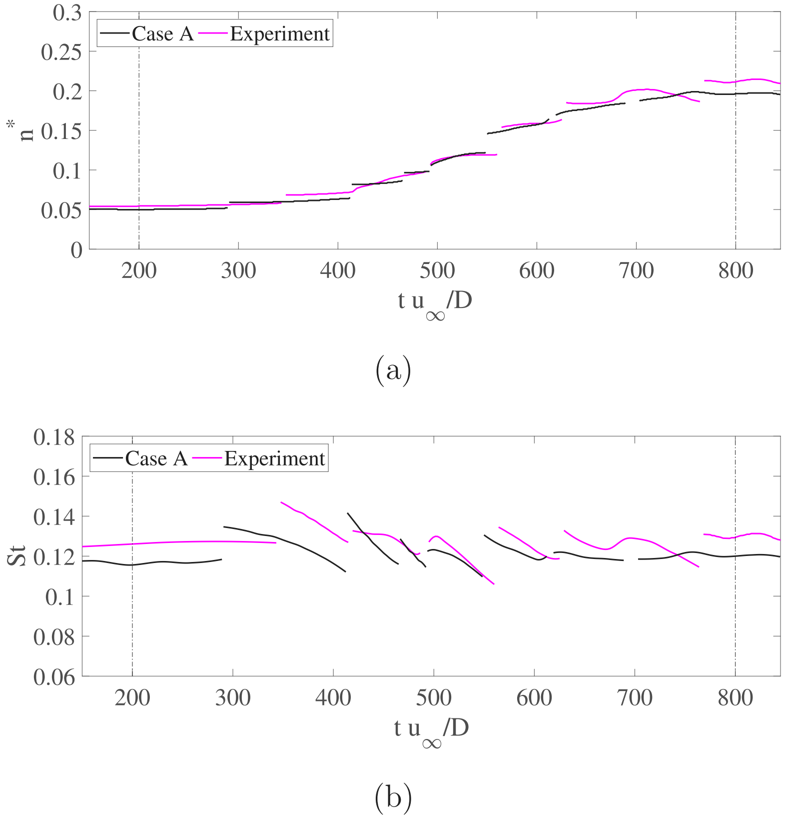

Fig. 8. Time–frequency analysis of $C_{\Delta P_L}$ signal during the accelerating flow in Case A: (b) vortex-shedding frequency (ridge of the wavelet energy map), and (c) Strouhal number. Experimental data from Brusco et al. (2022a).

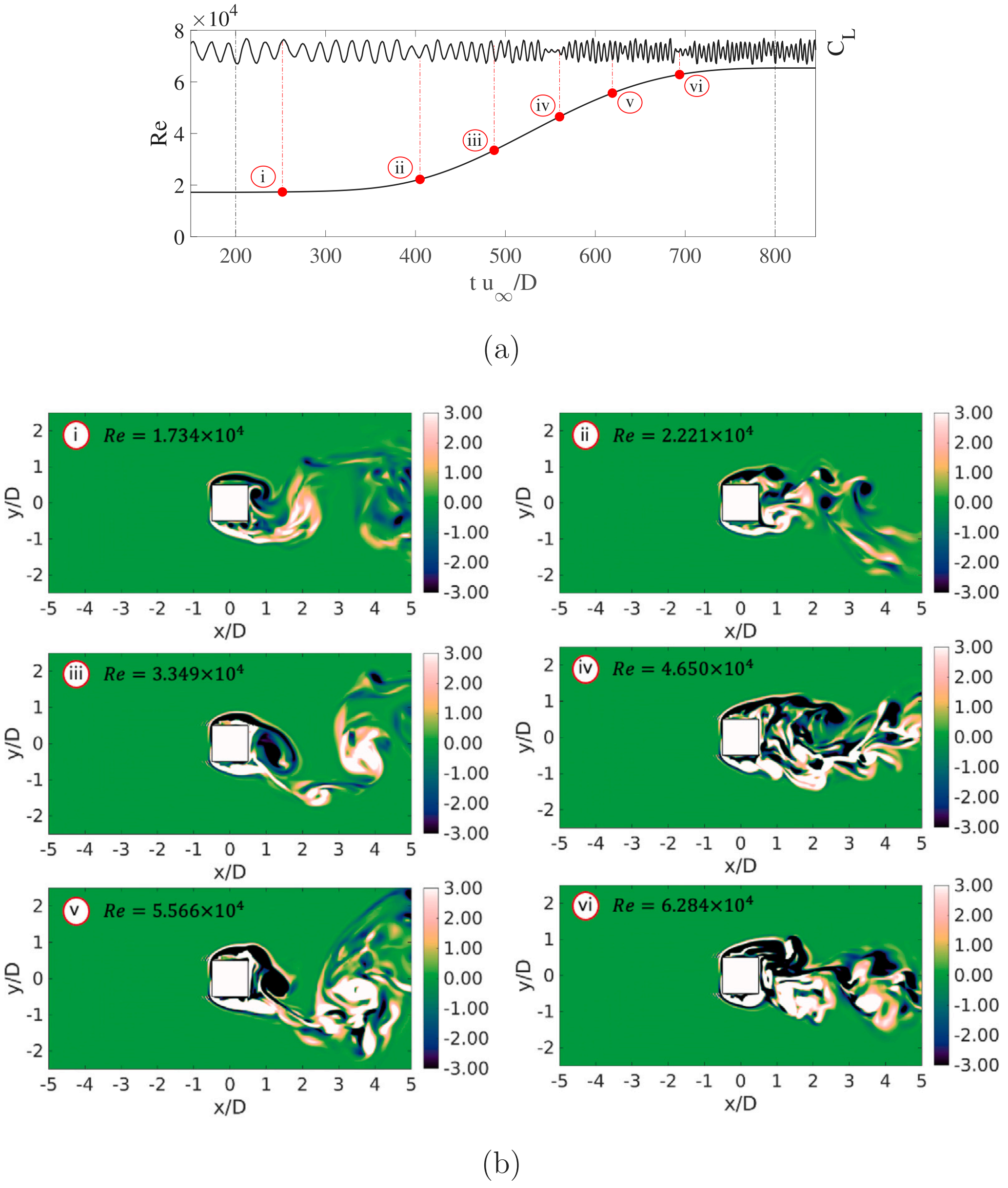

(a)

(b)

Fig. 9. (a) Time histories of Reynolds number and crossflow force coefficient during accelerating flow in Case A. (b) Spanwise-vorticity fields at section $z/D = 0$ at specific time instants: (i) $tu_\infty/D = 250.5$, (ii) $tu_\infty/D = 403.5$, (iii) $tu_\infty/D = 486.0$, (iv) $tu_\infty/D = 559.2$, (v) $tu_\infty/D = 618.1$, and (vi) $tu_\infty/D = 692.9$. See also the video in the Supplementary Material.

instants (ii), (iv), and (vi). During these time frames, the near wake becomes more symmetric, resulting in a significant decrease in crossflow force fluctuations. This supports thus the conjecture made in Brusco et al. (2022a) based on the analysis of differential pressure signals. Conversely, during instants (i), (iii), and (v), the alternating shedding of vortices is clearly observed. The topology of the vortex shedding seems to be qualitatively the same, i.e., the formation length and size of the vortices remain practically the same. The analysis of isocontours for the instantaneous vortex indicator λ_2 (Figs. 10 and 11) thoroughly validates these results, vividly illustrating the distinct nature of wakes during these specific time instants. In particular, in Fig. 11, for the instants at which there is vortex shedding, i.e., (i), (iii) and (v), vortical structures coherent the spanwise direction can be observed (blue contours). Conversely, in the remaining instants the vortex indicator loose any coherence in the spanwise direction, simply reflecting the corrugations of detaching shear layers.

The discontinuities in the vortex-shedding mechanism can be analyzed also by computing (i) the temporal behavior of the spanwise-averaged fluxes, ϕ, of the spanwise component of vorticity within the two shear layers detaching from the upstream edges and (ii) the variation in time of the dissipation, D_T, across the entire flow field. The fluxes ϕ_t and ϕ_b are calculated at the section $x/D = -0.4$ for $y/D \geq 0.5$ and $y/D \leq -0.5$, as follows:

$$\phi_t = \int_{y/D \geq 0.5} \omega_z u_x dy \tag{7}$$

$$\phi_b = \int_{y/D \leq -0.5} \omega_z u_x dy \tag{8}$$

where u_x is the streamwise component of the velocity.

The variation in dissipation, D_T, across the entire flow field is computed using the Bobyleff–Forsyth formula (Serrin, 1959), as presented

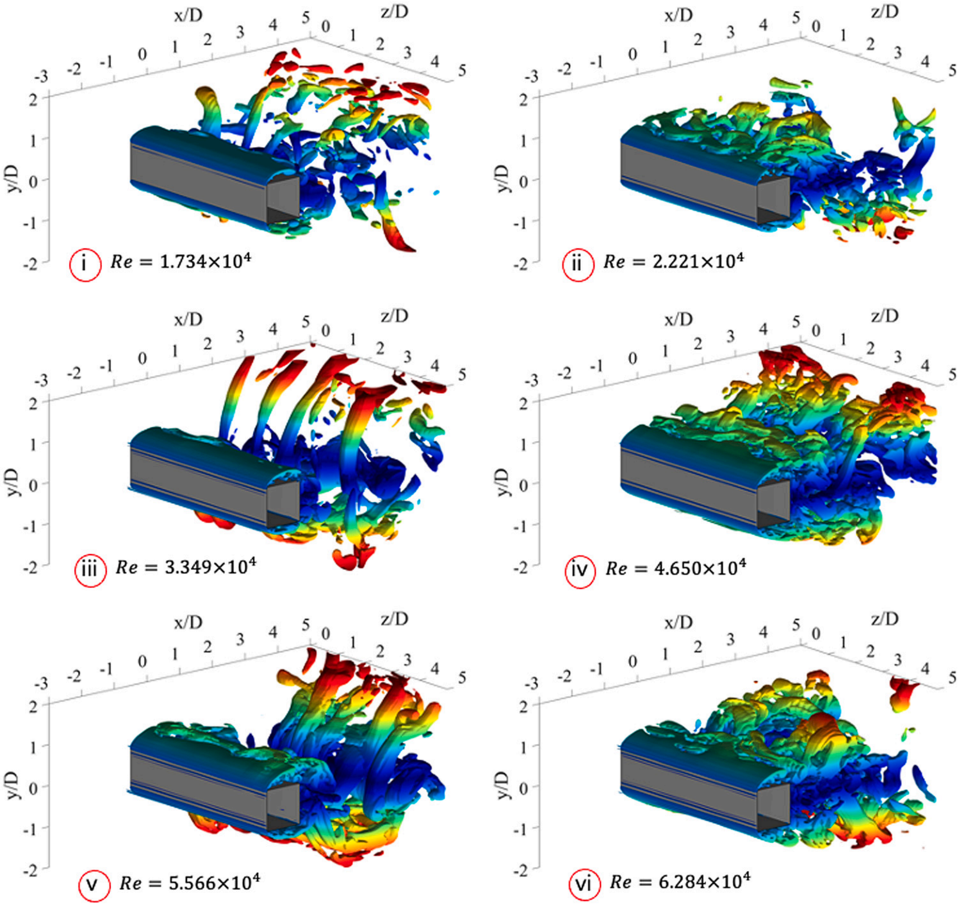

Fig. 10. Three-dimensional view of the isosurfaces of the instantaneous vortex-indicator λ_2 at specific time instants: (i) $tu_\infty/D = 250.5$, (ii) $tu_\infty/D = 403.5$, (iii) $tu_\infty/D = 486.0$, (iv) $tu_\infty/D = 559.2$, (v) $tu_\infty/D = 618.1$, and (vi) $tu_\infty/D = 692.9$. The isocontours are colored according to the y coordinate.

in the alternative formulation introduced by Buresti (2012):

$$D_T = \int_v \Phi dv = \mu \int_v \omega^2 dv - 2\mu \int_\Sigma \frac{\partial(p/\rho)}{\partial n} d\Sigma. \tag{9}$$

In this expression, which is applicable to incompressible flows, Φ denotes the dissipation function, v represents a general fluid volume of border Σ, ω^2 indicates enstrophy (the squared magnitude of the vorticity vector), μ stands for the viscosity of the fluid, and $\partial/\partial n$ signifies the derivative along the outer unit normal vector of Σ. It is crucial to emphasize that in Eq. (9), the second term is negligible compared to that of the first term. Consequently, variations in D_T are directly linked to the vorticity, specifically to ω_z.

As shown in Fig. 12a, the vorticity fluxes within the detaching shear layers increase with the rise in velocity. However, analogously with what observed from the aerodynamics coefficients, corresponding with discontinuities in the alternate vortex shedding, there are sudden drops in both the magnitude and the oscillations of the vorticity fluxes. The dissipation over time, D_T, illustrated in Fig. 12b, also experiences significant reductions during the vortex-shedding discontinuities, aligning with the simultaneous reduction in the drag coefficient (see Fig. 6b) and with a mitigated oscillation of the lift coefficient (see Fig. 5b).

A similar stepwise increase behavior of St has been found with increasing the chord-to-depth ratio in a flow around rectangular cylinders at constant velocity and low Reynolds number, e.g., by Tan et al. (1998) and Hourigan et al. (2001). The different Strouhal number steps shown therein represent various modes of shedding, and are conjectured to result from a feedback loop. This loop consists of vortices shed from the separating and reattaching shear layer at the leading edge, traversing the chord of the plate, interacting with the trailing edge, and generating a pressure pulse that travels upstream to excite and control the leading-edge separating shear layer. This process thereby locks subsequently shed leading-edge vortices. Therefore, we think that the physical phenomena characterizing the investigated case are quite different. Indeed, in the time intervals in which the vortex shedding is regular, the detaching shear layers directly roll-up in the Von Karman vortices in the wake without the presence of multiple vortices traveling over the cylinder surface. Conversely, in the considered case the stepwise behavior of St corresponds to an interruption of the vortex shedding, which subsequently resumes with a different frequency but a similar topology. The reasons of these periodic interruptions of the vortex shedding, thus, do not seem to be related to a lock-in phenomenon. On the other hand, they remain unclear and further investigations could be the object of future work.

6. Effect of the acceleration intensity

We now present the results for Cases B and C, characterized by higher acceleration intensities compared to Case A. The time evolution of the differential-pressure and force coefficients for the crossflow and streamwise directions is illustrated in Figs. 13 and 14, respectively. It is observed that the increase in acceleration intensity does not result in significant variations in the mean values and amplitude of fluctuations of the coefficients. Sudden reductions in the oscillation amplitudes of $C_{\Delta P_L}$ and C_L is also observed for Cases B and C (Fig. 13), indicating that

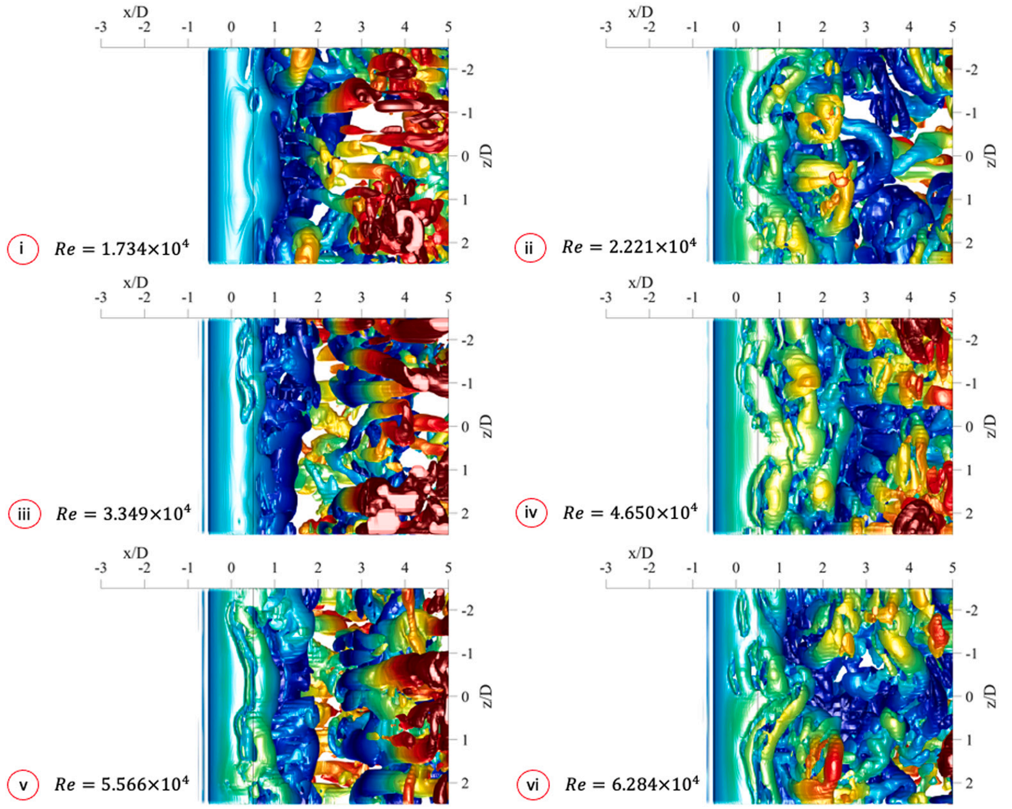

Fig. 11. Top view of the isosurfaces of the instantaneous vortex-indicator λ_2 at specific time instants: (i) $tu_\infty/D = 250.5$, (ii) $tu_\infty/D = 403.5$, (iii) $tu_\infty/D = 486.0$, (iv) $tu_\infty/D = 559.2$, (v) $tu_\infty/D = 618.1$, and (vi) $tu_\infty/D = 692.9$. The isocontours are colored according to the y coordinate.

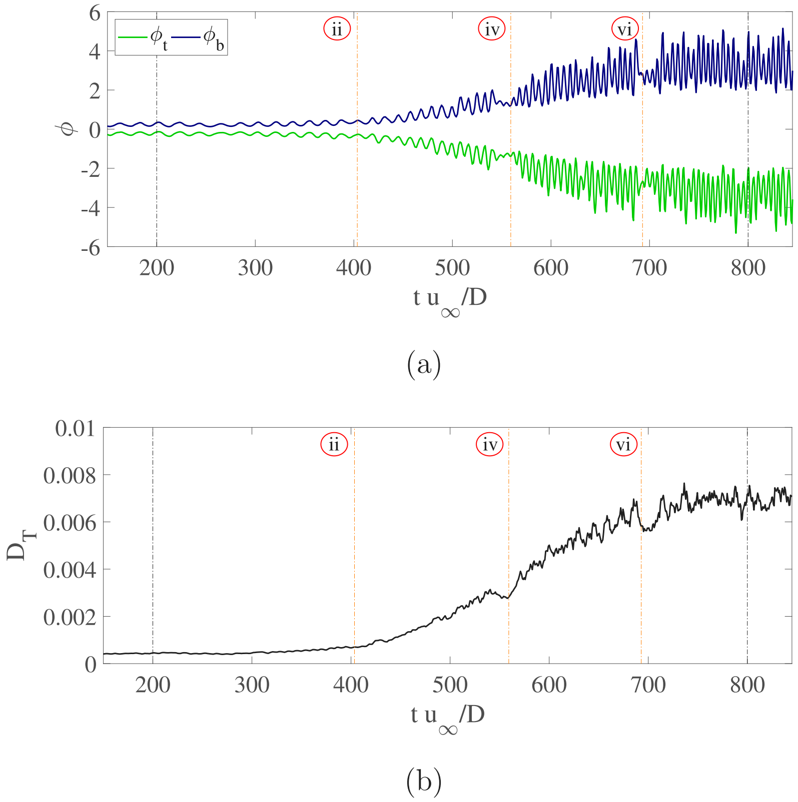

Fig. 12. Time histories of (a) the fluxes of the spanwise vorticity ϕ_t and ϕ_b and (b) the non-dimensional dissipation D_T.

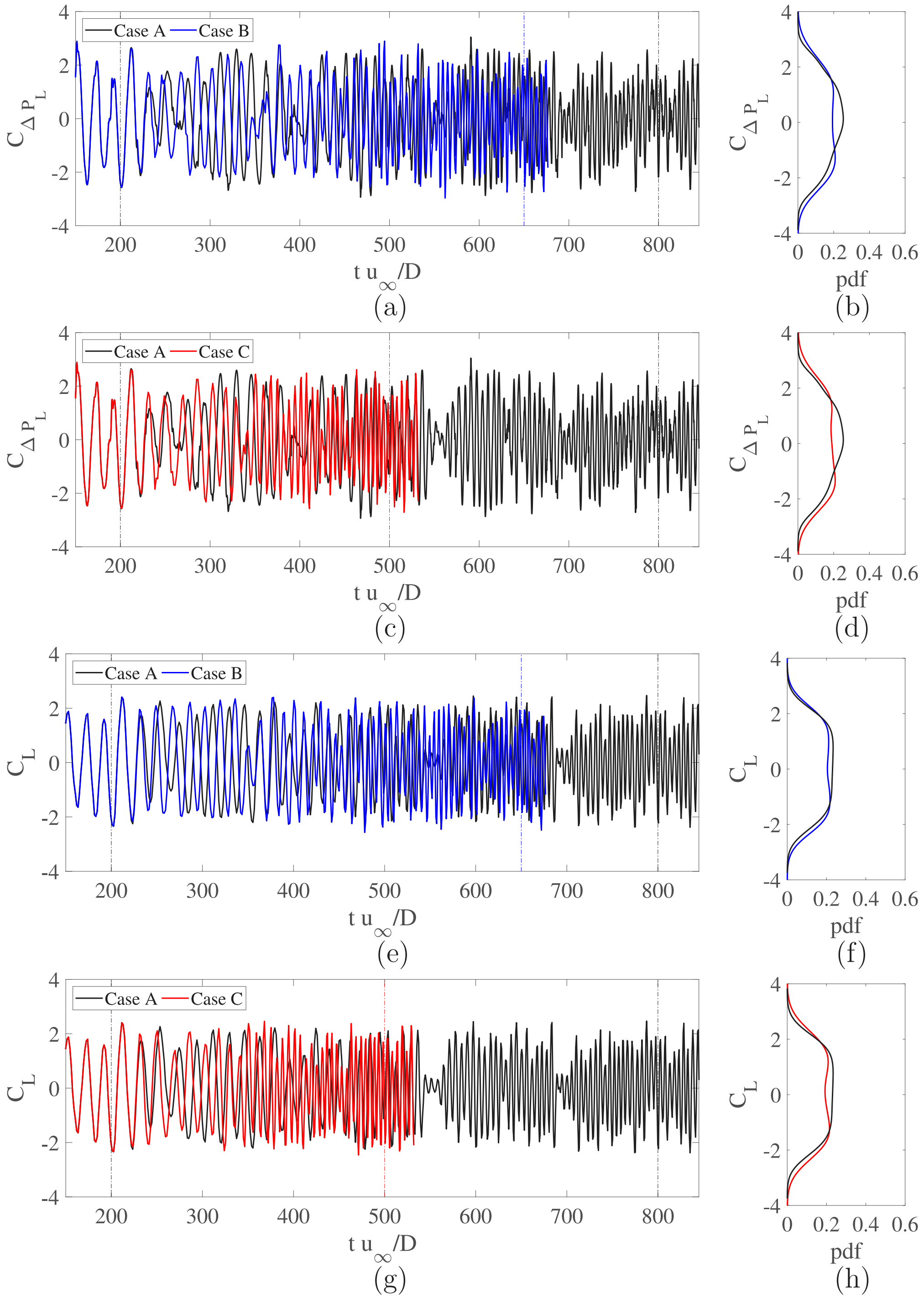

Fig. 13. Time histories of (a) $C_{\Delta P_L}$ for Case B, (c) $C_{\Delta P_L}$ for Case C, (e) C_L for Case B, and (g) C_L for Case C, along with the related probability density functions (b, d, f, h). Comparison with the results from Case A.

for all the acceleration intensities vortex packets are shed at a constant frequency interrupted by discontinuities in the vortex-shedding mechanism. The mean values of C_D do not significantly differ from those of Case A (see Fig. 15) and the standard deviations are similar for the three cases.

Time–frequency analyses are conducted on the crossflow force coefficient, C_L, signals. Consistent results are obtained for the $C_{\Delta P_L}$ signals, although they are not shown here for brevity. The ridges of wavelet energy maps are depicted in Fig. 16a. As previously found for Case A, also for Cases B and C the time-lengths of the constant-frequency time cells are lower near their respective acceleration maxima. The increasing acceleration intensities for Cases B and C result in shorter constant-frequency time cells. The frequency levels are approximately the same for the different cases, but they occur earlier in time. The effect of different acceleration intensities on the Strouhal number is illustrated in Fig. 16b. The slope of the St variation within the time cells increases with the acceleration intensity because the inflow velocity varies more steeply in time. The mean value, standard deviation, and overall variation of the Strouhal number during the accelerations are shown in Fig. 16c. The mean values align with the expected value

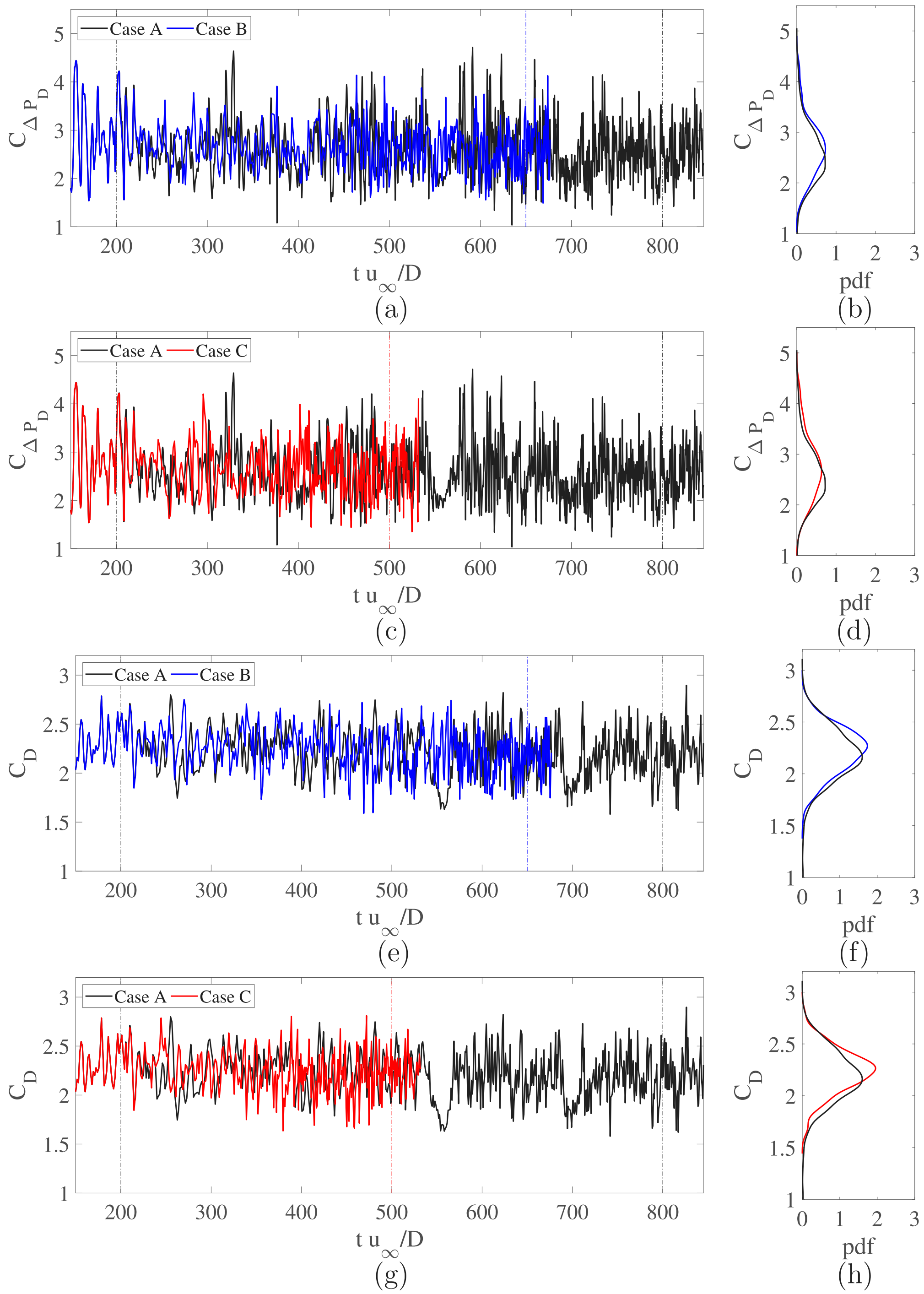

Fig. 14. Time histories of (a) $C_{\Delta P_D}$ for Case B, (c) $C_{\Delta P_D}$ for Case C, (e) C_D for Case B, and (g) C_D for Case C, along with the related probability density functions (b, d, f, h). Comparison with the results from Case A.

for steady inflow conditions (Section 4). However, considering a range of variation of plus and minus two standard deviations (at a 95% confidence level), a Strouhal number range of $St = 0.10{-}0.14$ characterizes the oscillating loads acting on the structure in accelerating-inflow conditions for all the three cases. Nonetheless, Case 3 seems to be characterized by a higher dispersion of the results, suggesting this effect as played by the inlet acceleration.

Given that the effect of acceleration intensity results in different time histories of the Reynolds number, Fig. 17 displays the vortex-shedding frequency and Strouhal number as functions of Re. The three

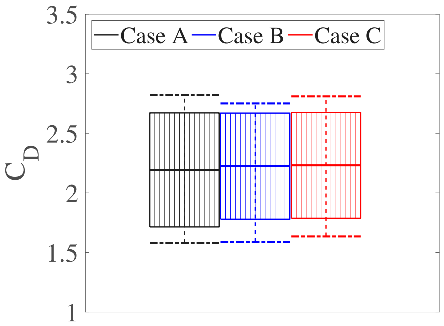

Fig. 15. Time-statistics of the variation of C_D for the different inflow accelerations. The rectangles represent the mean value plus or minus two times the standard deviation, while the lines above and below indicate the maximum extent of the variation.

curves for n^* and St collapse reasonably well into each other. In particular, St-Re behaviors are almost identical for all three accelerating flows, indicating that within the considered range of Gaussian acceleration intensities, the same flow dynamics occur when specific values of Re numbers are reached. When the Reynolds number variation exceeds certain values, a discontinuity in the vortex shedding occurs, leading to an abrupt frequency variation. Finally, the cells have roughly the same length in terms of Reynolds number interval, and the slopes of variation of St within each cell are similar for the different acceleration intensities.

7. Comparison between constant and Gaussian-type accelerations

The comparison between Case A and the constant acceleration is presented in Fig. 18 for the time histories of the streamwise force coefficient and the crossflow force coefficient, along with their associated pdfs. The mean streamwise forces are similar, and the amplitude variation of the crossflow force is nearly identical, as confirmed by the overlapping pdfs (Figs. 18b and 18d). Figs. 19a and 19b show the time behavior of the vortex shedding frequency (ridge of the wavelet energy map of the C_L signals) and Strouhal number during the two accelerations. Constant-frequency time cells are found for both accelerations, but they have different time lengths. Indeed, the presence of the constant-frequency time cells is evident independently of the adopted accelerating condition. The former and latter time instant of the constant accelerating condition are characterized by higher acceleration intensities compared to Case A, which lead to the presence of shorter time-cells. The slope of the Strouhal number is almost constant during the whole time history for the simulation with the constant value of the acceleration, and its range of variation does not differ from the one found for Case A, i.e., $0.10 \leq St \leq 0.14$. Figs. 20a and 20b compare the same quantities as a function of the Reynolds number. As previously observed for Gaussian-type accelerations of different intensities, the frequency and Strouhal number behaviors for Case A and for the constant acceleration almost overlap when plotted as a function of Re.

8. Conclusions

This paper investigated the impact of Gaussian-type inflow accelerations on the aerodynamic characteristics of a square cylinder through LES. A good agreement is found with the experiment conducted by Brusco et al. (2022a) for the reference acceleration (Case A). Wavelet time–frequency analyses on LES signals confirm the presence of time cells, wherein the vortex shedding frequency remains almost constant. These cells are delineated by an interruption of the alternate vortex shedding, resulting in a significant weakening of crossflow force fluctuations along with a reduction in vorticity fluxes within the detaching shear layers and dissipation in the flow field. The duration of the cells is shorter near the acceleration peak, where the velocity variation is higher. The Strouhal number significantly varies within the constant-frequency time intervals, due to the variation of the inflow velocity. The mean value of the Strouhal number is practically the same as the one characterizing the same flow in steady inlet conditions for the considered range of Reynolds numbers. However, a variation over time of ±20% is observed. This aspect could potentially influence the wind-induced loading of slender structures during thunderstorm conditions, suggesting that it should be taken into consideration in their design. Regarding the effect of the acceleration intensity, the behavior is qualitatively the same, but the constant-frequency cells become shorter, and the variation of the Strouhal within the cells steeper as the acceleration increases. However, St exhibits reasonably the same behavior for all acceleration intensities when plotted as a function of Re. A similar analysis could be repeated in the future for different shapes of the cylinder cross-section and variations in inflow velocity, considering also decelerating inflow conditions, which are interesting because hysteresis and lock-in phenomena could take place. Moreover, the effect of the free-stream turbulence should also be investigated as a future perspective. Finally, despite the present research focusing on the vortex-shedding phenomenon and being carried out only for static tests and a single wind incidence (0 degrees), there is potential interest in planning further research to investigate the galloping phenomenon under transient conditions.

CRediT authorship contribution statement

G. Lunghi: Writing – original draft, Visualization, Software, Methodology, Investigation, Data curation. **S. Brusco:** Writing – original draft, Visualization, Validation, Investigation, Data curation, Conceptualization. **A. Mariotti:** Writing – review & editing, Supervision, Methodology, Investigation, Data curation, Conceptualization. **G. Piccardo:** Writing – review & editing, Supervision, Conceptualization. **M.V. Salvetti:** Writing – review & editing, Supervision, Investigation, Conceptualization.

Declaration of competing interest

The authors declare that they have no known competing financial interests or personal relationships that could have appeared to influence the work reported in this paper.

Data availability

Data will be made available on request.

Acknowledgments

The authors express sincere gratitude to Prof. Guido Buresti for his invaluable suggestions. We acknowledge the CINECA award under the ISCRA initiative, for the availability of high-performance computing resources and support (ISCRA Project: IscC_THUNDERC). This work is supported by PNRR M4C2 - HPC, Big data and Quantum Computing (Simulazioni, calcolo e analisi dei dati e altre prestazioni - CN1) - CUP I53C22000690001 SPOKE 6 Multiscale modelling & Engineering applications and by the National Recovery and Resilience Plan (NRRP).

Appendix A. Supplementary data

Supplementary material related to this article can be found online at https://doi.org/10.1016/j.jweia.2024.105814.

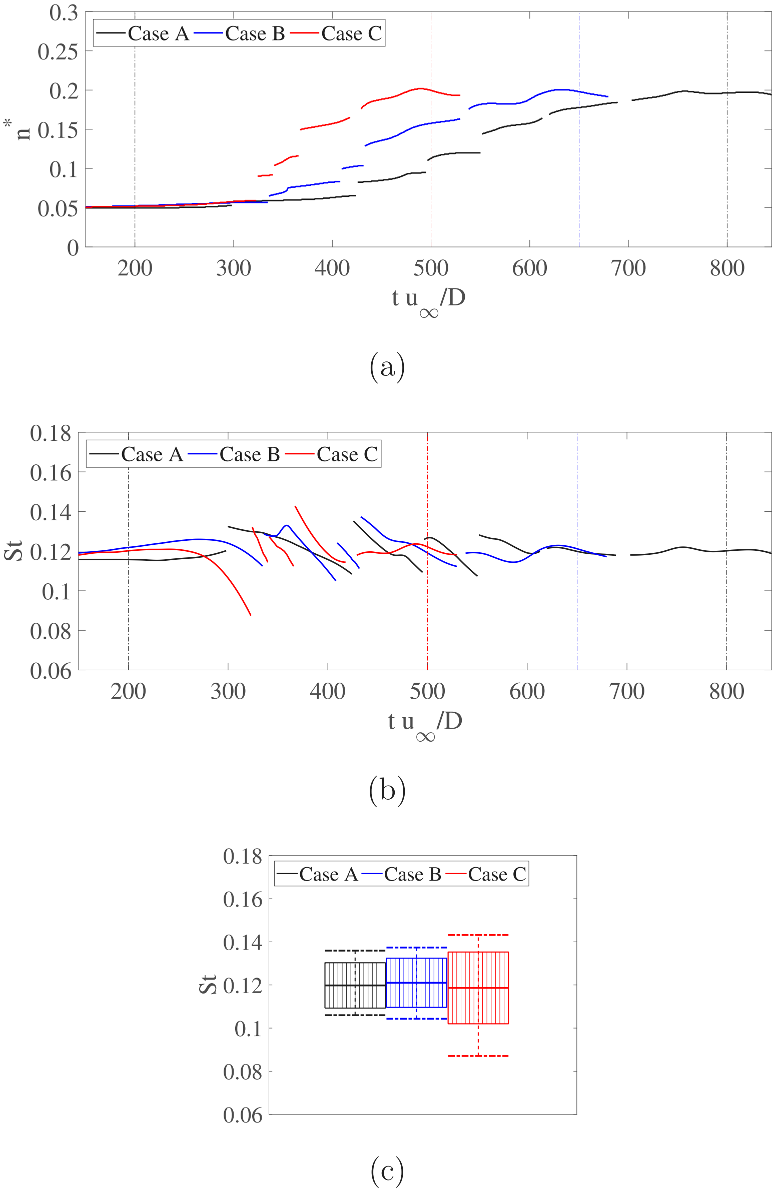

Fig. 16. Time–frequency analysis of C_L signals during the accelerating flow: (a) vortex-shedding frequencies (ridges of the wavelet energy map), (b) Strouhal numbers, and (c) time-statistics of the variation of the Strouhal number (the rectangles represent the mean value plus or minus two times the standard deviation, while the lines above and below indicate the maximum extent of the variation).

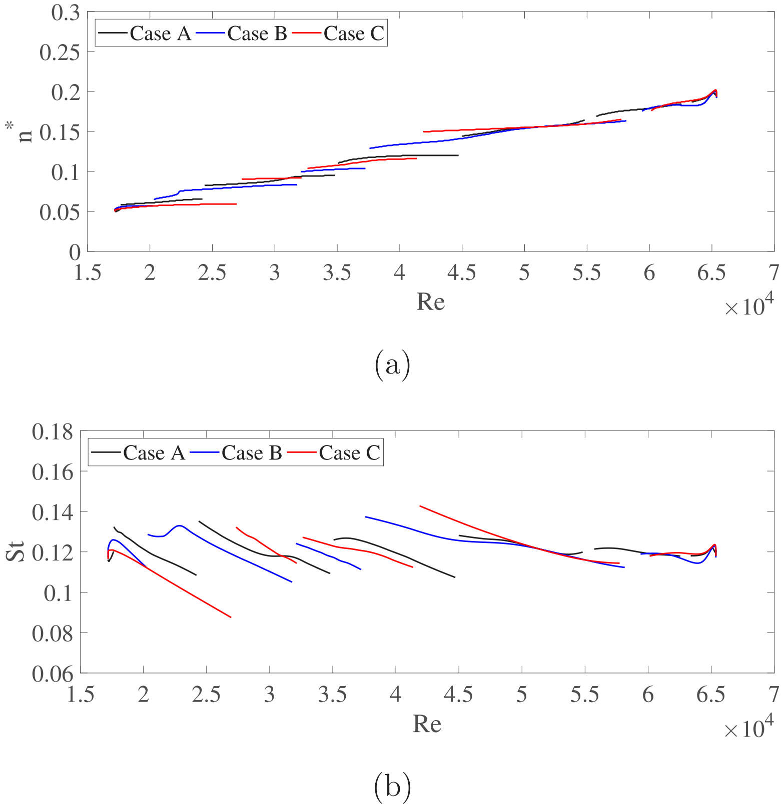

(a)

(b)

Fig. 17. Effect of the Reynolds number on (a) the vortex-shedding frequency and (b) Strouhal number for the different inflow accelerations.

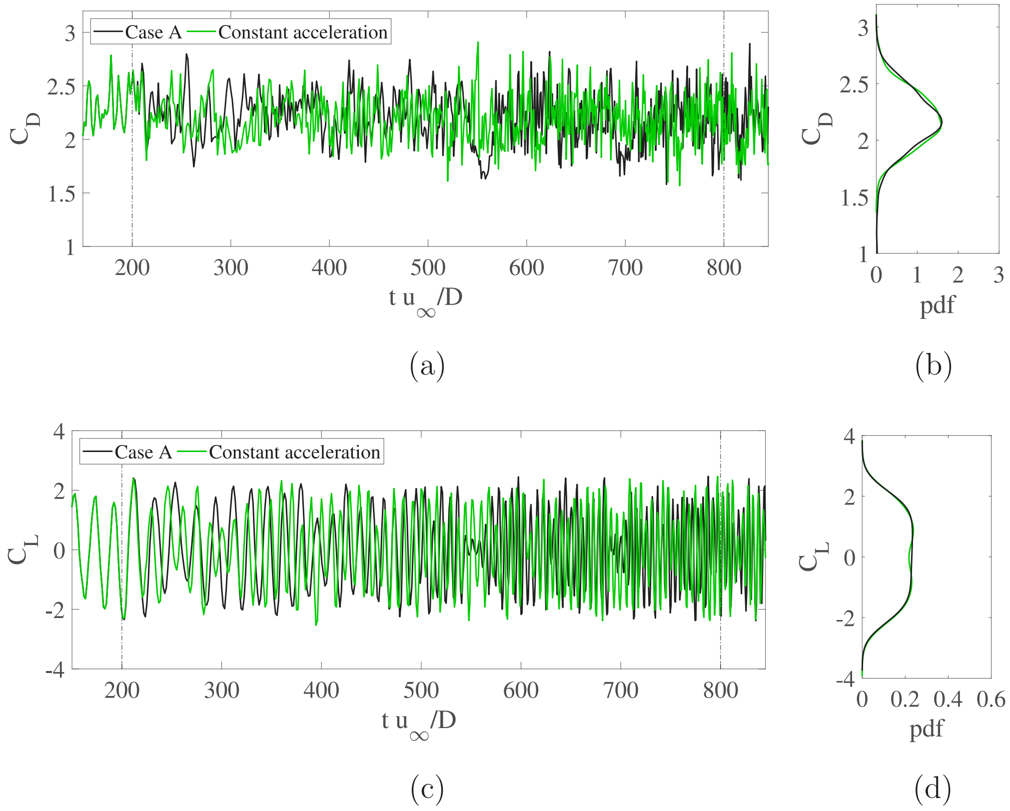

(a) (b)

(c) (d)

Fig. 18. Time histories of (a) the streamwise force coefficient, (d) along with the associated probability density function, and (c) the crossflow force coefficient, (d) along with the associated probability density function, during accelerating flow for the Gaussian-type accelerating flow of Case A and the constant acceleration.

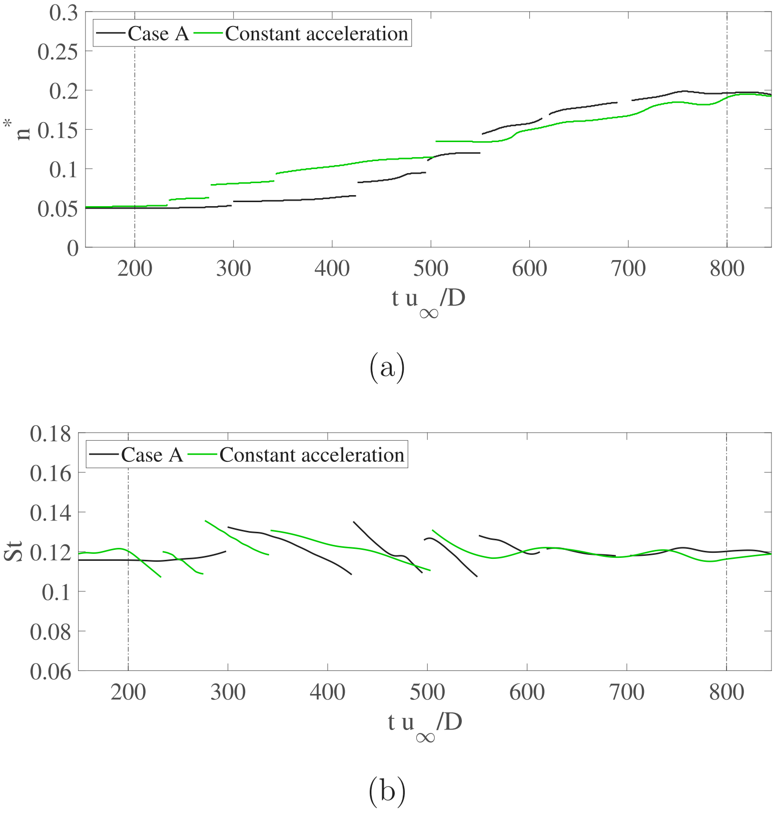

Fig. 19. Time–frequency analysis of C_L signals during the accelerating flow: (a) vortex-shedding frequencies (ridges of the wavelet energy map) and (b) Strouhal numbers.

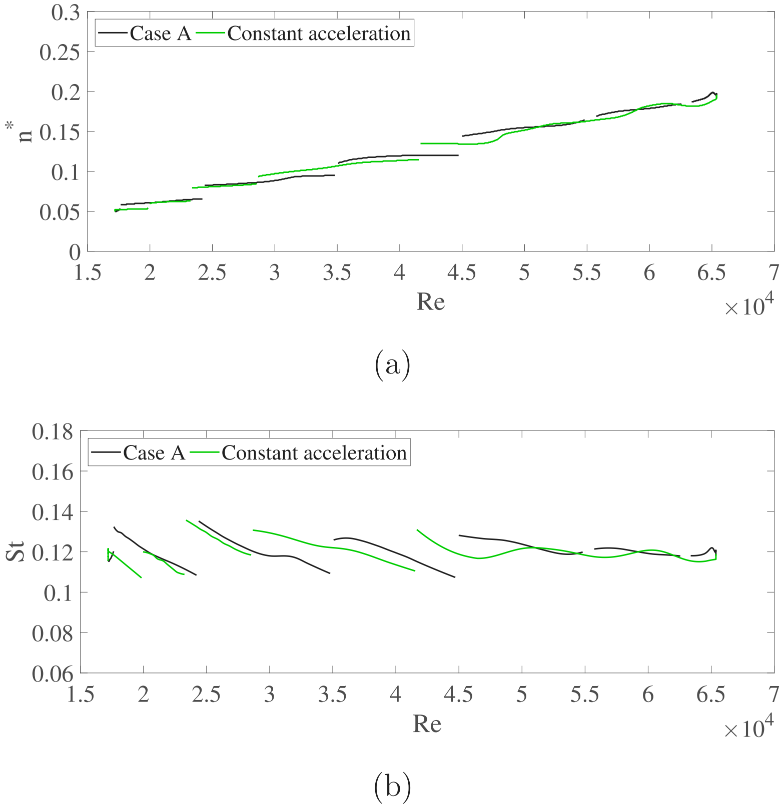

Fig. 20. Effect of the Reynolds number on (a) the vortex-shedding frequency and (b) Strouhal number for the different inflow accelerations.

References

Bearman, P.W., Obasaju, E.D., 1982. Experimental study of pressure fluctuations on fixed and oscillating square-section cylinders. J. Fluid Mech. 119, 297–321.

Bearman, P.W., Trueman, D.M., 1972. An investigation of the flow around rectangular cylinders. Aeronaut. Quart. 23 (3), 229–237.

Bruno, L., Oberto, D., 2022. Effects of cell quality in grid boudary layer on the simulated flow around a square cylinder. Comput. & Fluids 238, 105351.

Brusco, S., Bin, H.Y., Lo, Y.L., Piccardo, G., 2024. Transient aerodynamics of a square cylinder under downburst-like accelerating flows reproduced in a multiple-fan wind tunnel. J. Fluids Struct. 124, 104038.

Brusco, S., Buresti, G., Lo, Y.-L., Piccardo, G., 2022a. Constant-frequency time cells in the vortex-shedding from a square cylinder in accelerating flows. J. Wind Eng. Ind. Aerodyn. 230, 105182.

Brusco, S., Buresti, G., Piccardo, G., 2022b. Thunderstorm-induced mean wind velocities and accelerations through the continuous wavelet transform. J. Wind Eng. Ind. Aerodyn. 221, 104886.

Buresti, G., 2012. Elements of fluid dynamics. Imp. Coll. Press.

Buresti, G., Lombardi, G., Bellazzini, J., 2004. On the analysis of fluctuating velocity signals through methods based on the wavelet and Hilbert transforms. Chaos Solitons Fractals 20, 149–158.

Carmona, R., Hwang, W.-L., Torresani, B., 1998. Practical Time-Frequency Analysis. Academic Press, San Diego, CA.

Chen, J.M., Liu, C.H., 1999. Vortex shedding and surface pressures on a square cylinder at incidence to a uniform air stream. Int. J. Heat Fluid Flow 20, 592–597.

Davenport, A.G., 1961. The application of statistical concepts to the wind loading of structures. Proc. Inst. Civ. Eng. 19 (4), 449–472.

Domarazdki, J.A., 2010. Large eddy simulations without explicit eddy viscosity models. Int. J. Comput. Fluid Dyn. 24 (10), 435–447.

Durão, D.F.G., Heitor, M.V., Pereira, J.C.F., 1988. Measurements of turbulent and periodic flows around a square cross-section cylinder. Exp. Fluids 6 (5), 298–304.

Fischer, P., Mullen, J., 2001. Filter-based stabilization of spectral element methods. C. R. Acad. Sci., Paris I 332 (1), 265–270.

Guo, F., Wu, G., Du, X., Mason, M.S., 2021. Numerical investigation of flow around a square cylinder in accelerated flow. Phys. Fluids 33 (10), 104105.

Hourigan, K., Thompson, M.C., Tan, B.T., 2001. Self-sustained oscillations in flows around long blunt plates. J. Fluids Struct. 15, 387–398.

Jeong, J., Hussain, F., 1995. On the identification of a vortex. J. Fluid Mech. 285, 69–94.

Kareem, A., Wu, T., 2013. Wind-induced effects on bluff bodies in turbulent flows: Nonstationary, non-Gaussian and nonlinear features. J. Wind Eng. Ind. Aerodyn. 122, 21–37.

Kawai, H., 1983. Pressure fluctuations on square prisms – Applicability of strip and quasi-steady theories. J. Wind Eng. Ind. Aerodyn. 13, 197–208.

Kopp, G.A., Wu, C.H., 2020. A framework to compare wind loads on low-rise buildings in tornadoes and atmospheric boundary layers. J. Wind Eng. Ind. Aerodyn. 204, 104269.

Kwon, D.K., Kareem, A., 2019. Towards codification of thunderstorm/downburst using gust front factor: Model-based and data-driven perspectives. Eng. Struct. 199 (11), 109608.

Lee, B.E., 1975. The effect of turbulence on the surface pressure field of square prisms. J. Fluid Mech. 69, 263–282.

Li, Y., Mason, M.S., Bin, H.-Y., Lo, Y.-L., 2023. Aerodynamic characteristics of a high-rise building in a steady thunderstorm outflow-like flow field. J. Wind Eng. Ind. Aerodyn. 240, 105501.

Lunghi, G., Pasqualetto, E., Rocchio, B., Mariotti, A., Salvetti, M.V., 2022. Impact of the lateral mean recirculation characteristics on the near wake and bulk quantities of the BARC configuration. Wind Struct. 34 (1), 115–125.

Lyn, D., Einav, S., Rodi, W., Park, J.A., 1995. Laser doppler velocimetry study of ensemble averaged characteristics of the turbulent near wake of a square cylinder. J. Fluid Mech. 304, 285–319.

Lyn, D.A., Rodi, W., 1994. The flapping shear layer formed by flow separation from the forward corner of a square cylinder. J. Fluid Mech. 267, 353–376.

Maday, Y., Patera, A.T., Rønquist, E.M., 1990. An operator-integration-factor splitting method for time-dependent problems: Application to incompressible fluid flow. J. Sci. Comput. 5 (4), 263–292.

Mariotti, A., 2018. Axisymmetric bodies with fixed and free separation: Base-pressure and near-wake fluctuations. J. Wind Eng. Ind. Aerodyn. 176, 21–31.

Mariotti, A., Siconolfi, L., Salvetti, M.V., 2017. Stochastic sensitivity analysis of large-eddy simulation predictions of the flow around a 5:1 rectangular cylinder. Eur. J. Mech. B Fluids 62, 149–165.

Minguez, M., Brun, C., Pasquetti, R., Serre, E., 2011. Experimental and high-order LES analysis of the flow in near-wall region of a square cylinder. Int. J. Heat Fluid Flow 32 (3), 558–566.

Nakamura, Y., Ohya, Y., 1984. Effects of turbulence on the mean flow past two dimensional rectangular cylinders. J. Fluid Mech. 149, 255–273.

Norberg, C., 1993. Flow around rectangular cylinders: Pressure forces and wake frequencies. J. Wind Eng. Ind. Aerodyn. 49(1–3), 187–196.

Petty, D.G., 1979. The effect of turbulence intensity and scale on the flow past square prisms. J. Wind Eng. Ind. Aerodyn. 4 (3-4), 247–252.

Roberson, J.A., Lin, C.Y., Rutherford, G.S., Stine, M.D., 1972. Turbulence effects on drag of sharp-edged bodies. J. Hydraul. Div. 98 (7), 1187–1203.

Rocchio, B., Mariotti, A., Salvetti, M.V., 2020. Flow around a 5:1 rectangular cylinder: Effects of upstream-edge rounding. J. Wind Eng. Ind. Aerodyn. 204, 104237.

Rodi, W., 1997. Comparsion of LES and RANS calculations of the flow around bluff bodies. J. Wind Eng. Ind. Aerodyn. 69–71, 55–75.

Rodi, W., Ferziger, J.H., Breuer, M., Pourquié, M., 1997. Status of large eddy simulation: Results of a workshop. J. Fluids Eng. Trans. ASME 119 (2), 248–262.

Romanic, D., Ballestracci, A., Canepa, F., Solari, G., Hangan, H., 2021. Aerodynamic coefficients and pressure distribution on two circular cylinders with free end immersed in experimentally produced downburst-like outflows. Adv. Struct. Eng. 24 (3), 522–538.

Saha, A.K., Biswas, G., Muralidhar, K., 2003. Three-dimensional study of flow past a square cylinder at low Reynolds numbers. J. Heat Fluid Flow 24 (1), 54–66.

Sarpkaya, T., 1963. Lift, drag, and mass coefficients for a circular cylinder immersed in time dependent flow. J. Appl. Mech. 30, 13–15.

Sarpkaya, T., 1966. Separated flow about lifting bodies and impulsive flow about cylinders. AIAA J. 4, 414–420.

Sarpkaya, T., Ihrig, C., 1986. Impulsively started steady flow about rectangular prisms: Experiments and discrete vortex analysis. J. Fluids Eng. 108, 47–54.

Sarpkaya, T., Kline, H., 1982. Impulsively-started flow about four types of bluff body. J. Fluids Eng. 104, 207–213.

Serrin, J., 1959. Mathematical principles of classical fluid mechanics. In: Flügge, S. (Ed.), Handbuch der Physik VIII/1. Springer, pp. 125–263.

Sohankar, A., 2006. Flow over a bluff body from moderate to high Reynolds numbers using large eddy simulation. Comput. & Fluids 35 (10), 1154–1168.

Sohankar, A., Norberg, C., Davidson, L., 1999. Simulation of three-dimensional flow around a square cylinder at moderate Reynolds numbers. Phys. Fluids 11, 288–306.

Solari, G., 2019. Wind Science and Engineering. Springer Nature Switzerland.

Solari, G., 2020. Thunderstorm downburst and wind loading of structures: Progress and prospect. Front. Built Env. 6 (63), 1–24.

Takeuchi, T., Maeda, J., 2013. Unsteady wind force on an elliptic cylinder subjected to a short-rise-time gust from steady flow. J. Wind Eng. Ind. Aerodyn. 122, 138–145.

Takeuchi, T., Maeda, J., Kawashita, H., 2008. The overshoot of aerodynamic forces on a railcar-like body under step-function-like gusty winds. In: Proceedings of the 6th International Colloquium on Bluff Body Aerodynamics and Applications. Milano, Italy, pp. 20–24.

Tamura, T., Miyagi, T., 1999. The effect of turbulence on aerodynamic forces on a square cylinder with various corner shapes. J. Wind Eng. Ind. Aerodyn. 83 (1-3), 135–145.

Tan, B.T., Thompson, M.C., Hourigan, K., 1998. Simulated flow around long rectangular plates under cross flow perturbations. Int. J. Fluid Dyn. 2, 1.

Trias, F.X., Gorobets, A., Oliva, A., 2015. Turbulent flow around a square cylinder at Reynolds number 22,000: A DNS study. Comput. & Fluids 123, 87–98.

Vickery, B.J., 1966. Fluctuating lift and drag on a long square cylinder of square cross section in a smooth and in a turbulent stream. J. Fluid Mech. 25, 481–494.

Yang, T., Mason, M.S., 2019. Aerodynamic characteristics of rectangular cylinders in steady and accelerating wind flow. J. Fluids Struct. 90, 246–262.

Zhou, D., Xia, C., Wu, L., Meng, S., 2023. Effect of the wind speed on aerodynamic behaviours during the acceleration of a high-speed train under crosswind. J. Wind Eng. Ind. Aerodyn. 232, 105287.